Projected near-term changes in three types of heat waves over China under RCP4.5

Article

Accepted Version

It is advisable to refer to the publisher's version if you intend to cite from the work. See Guidance on citing.

www.reading.ac.uk/centaur

CentAUR

1 **Projected near-term changes in three types of heat waves over China**

2 **under RCP4.5**

3 Su Qin[1] and Buwen Dong[2]

5 [1] Department of Atmospheric Sciences, Yunnan University, Kunming, China

6 [2] National Centre for Atmospheric Science-Climate, Department of Meteorology,

7 University of Reading, Reading, UK

21 Corresponding author:

22 Qin Su,

23 Department of Atmospheric Sciences,

24 Yunnan University,

25 Kunming, 650091, China

26 E-mail: suqin@ynu.edu.cn

Abstract

The future changes in three aspects of frequency, intensity, and duration of the compound, daytime, and nighttime heat waves (HWs) over China during extended summer (May–September) in a future period of the mid-21st century (FP; 2045-2055) under RCP4.5 scenario relative to present day (PD; 1994-2011) are investigated by two models, i.e. MetUM-GOML1 and MetUM-GOML2, comprising the atmospheric components of two state-of-the-art climate models coupled to a multi-level mixed-layer ocean model. The results show that all three types of HWs over China will occur more frequently with strengthened intensity and elongated duration in the mid-21st century. The compound HWs will change most dramatically with the frequency in the FP being 4-5 times that in the PD, and the intensity and duration doubling those in the PD. The changes of daytime and nighttime HWs are also remarkable, with the changes of nighttime HWs larger than those of daytime HWs. The future changes of the three types of HWs over China in two models are similar in terms of spatial patterns and area averaged quantities, indicating these projected changes of HWs over the China under RCP4.5 scenario are robust. The further analyses suggest that projected future changes of HWs over China are predominantly determined by the increase in seasonal mean surface air temperatures with change in temperature variability playing a minor role. The seasonal mean temperature increases are partly due to the increase in surface downward longwave radiation and partly due to the increase in surface shortwave radiation. The increased downward longwave radiation results from the enhanced greenhouse effect and the increased water vapor in the atmosphere. The increased

50 surface shortwave radiation results from the decreased aerosol emissions via direct

51 aerosol-radiation interaction and indirect aerosol-cloud interaction over southeastern

52 and northeastern China and the decreased cloud cover related to reduced relative

53 humidity.

54 **Key words:** heat waves, heat wave types, future changes, China, coupled models.

1. Introduction

56   Heat waves are usually defined as abnormally hot weather lasting for several days

57 (Perkins and Alexander 2013; Perkins 2015). This distinct type of extreme temperature

58 events has caused substantial damages to socioeconomics and human health (e.g.

59 Robine et al. 2008; Coumou and Rahmstorf 2012; Hatfield and Prueger 2015; Lesk et

60 al. 2016). In recent two decades, heat waves have occurred more frequently all over the

61 world (e.g., Meehl and Tebaldi 2004; Seneviratne et al. 2014). Without any exception,

62 several severe heat waves hit China recently in different regions and broke the regional

63 historical temperature records, such as the 2013 July-August heat wave in the lower

64 reaches of Yangtze River Valley (Sun et al. 2014; Zhou et al. 2014b; Ma et al. 2017),

65 the 2015 summer heat wave in western China (Sun et al. 2016), and the 2017 July heat

66 wave in central eastern China (Chen et al. 2018; Sparrow et al. 2018). These

67 catastrophic events led to enormous economic loss and heat-related morbidity and

68 mortality in China (e.g., Tan et al. 2007; Sun et al. 2016; Ma et al. 2017). The increased

69 occurrence of heat waves largely results from the increased mean temperature (Argueso

70 et al. 2016; Su and Dong 2019). As the increase in mean temperature will go on, how

3

71 the heat waves will change in the future under the global warming scenario is an

72 important issue for developing climate adaptation strategies.

73   A heat wave could take place on daytime, nighttime, or both. With different timing

74 of occurrence, the heat waves are related to different mechanisms and of different

75 impacts (Gershunov et al. 2009, Freychet et al. 2017). The heat waves in the day, usually

76 associated with dry conditions (Black et al. 2004; Gershunov et al. 2009; Wang et al.

77 2016), have a variety of disastrous impacts on infrastructures, ecosystem, and human

78 life (Wilbanks et al. 2012), while the heat waves at night, related to wet conditions

79 (Gershunov et al. 2009; Chen and Lu 2014), have relatively weak impact. However,

80 with the hot nights enhancing the damages of daytime high temperatures on human

81 health (Gosling et al 2009), the heat waves persisting throughout the day and night are

82 the most disastrous among these three types of heat waves (Karl and Knight 1997).

83 Thus, recent studies applied a more precise classification of heat waves according to

84 the timing of their occurrence to get more insights, which divided the heat waves into

85 three types, i.e., daytime, nighttime and compound ones (e.g., Chen and Li 2017; Chen

86 and Zhai 2017; Freychet et al. 2017; Su and Dong 2019).

87   In recent decades since the mid-20th century, the previously-defined heat waves,

88 which only consider the daytime temperatures and involve the daytime heat waves and

89 part of the compound heat waves, show increasing frequency and duration over China

90 (Li et al. 2017; Luo and Lau 2017; Wang et al. 2017; You et al. 2017). Some recent

91 studies, using the precisely defined daytime, nighttime, and compound heat waves over

4

92   most part of China, show significant increasing trends in frequency, intensity, and

93   duration (Chen and Zhai 2017; Freychet et al. 2017). Particularly, the increase of

94   frequency and intensity in compound and nighttime heat waves is much greater than

95   that in daytime ones (Chen and Li 2017; Chen and Zhai 2017; Su and Dong 2019). The

96   anthropogenic influences are highlighted to play crucial roles in the sharp increase in

97   occurrence of the heat waves over China (e.g., Wilcox et al. 2015; Freychet et al. 2018).

98   In more detail, Su and Dong (2019) reported that the increase in greenhouse gas

99   concentration is responsible for the decadal increase in frequency, intensity, and spatial

100   extent of the three types of heat waves over China across mid-1990s and the changes in

101   anthropogenic aerosol emission lead to the increase in frequency and intensity of the

102   daytime heat waves over Northeastern China and decrease the frequency and intensity

103   of daytime HWs over Southeastern China.

104   Considering the anthropogenic influences, future changes in the heat waves and

105   temperature extremes over China are assessed under different scenarios. There would

106   be an increase in warm extremes and a decrease in cold extremes under a warming

107   climate (Zhou et al. 2014a; Yu et al. 2018). The frequency and duration of previously-

108   defined heat waves over China would increase and the increase would become larger

109   when the mean temperature gets greater (Guo et al. 2017). However, only the future

110   changes in previously-defined heat waves are estimated and the assessment of future

111   changes in precisely defined compound, daytime, and nighttime heat waves is still

112   lacking. Meanwhile all above projections have used fully coupled general circulation

113   models (CGCMs). However, these CGCMs exhibit significant biases in simulated sea

surface temperature that challenge the reliability of climate projections (Wang et al.

2014).

Therefore, the main aims of this work are to estimate the future changes of the

daytime, nighttime, and compound heat waves over China and to reveal the associated

physical processes by using two near-globally coupled models comprising the

atmospheric components of two state-of-the-art climate models coupled to a multi-level

mixed-layer ocean and having a much smaller bias in simulated sea surface temperature

(Hirons et al. 2015, Dong et al. 2017, Luo et al. 2018). The structure of this paper is

organized as follows: The model and experiments are described in Section 2. Model

simulated extended seasonal mean surface air temperatures and definition of HWs are

described in Section 3. The projected changes in the three types of heat waves are shown

in Section 4. The physical processes responsible for future changes in heat waves are

illustrated in Section 5. Conclusions are summarized in Section 6.

2. Models and experiments

2.1 Models

Two coupled models, MetUM-GOML1 and MetUM-GOML2 (Hirons et al. 2015),

that comprise the atmospheric components of two state-of-the-art climate models

coupled to a multi-level mixed-layer ocean model, are used in this study. The

atmospheric component for MetUM-GOML1 is the Met Office Unified Model

(MetUM) at the fixed scientific configuration Global Atmosphere 3.0 (GA3.0; Arribas

et al. 2011; Walters et al. 2011). The atmospheric component for MetUM-GOML2 is

135 the MetUM GA6.0. The largest change in GA6.0 is that the "New Dynamics"

136 dynamical core is replaced with "ENDGame" (Walters et al. 2014). ENDGame

137 maintains the benefits of "New Dynamics", whilst improving its accuracy, stability and

138 scalability. The improved accuracy significantly reduces the model's implicit damping,

139 leading to a beneficial improvement to various modes of variability, such as the vertical

140 height of extra-tropical cyclones and the structure of frontal systems. The details about

141 GA6.0 are described in Walters et al. 2017. The resolution for these two atmospheric

142 models is 1.875° longitude by 1.25° latitude with 85 vertical layers. The models include

143 an interactive tropospheric aerosol scheme, which is able to simulate the direct, indirect

144 and semi-direct effects of aerosols (Walters et al. 2011; Jones et al. 2011). The oceanic

145 components for MetUM-GOML1 and MetUM-GOML2 are the same, which is a Multi-

146 Column K Profile Parameterization (MC-KPP) mixed-layer ocean model. The

147 horizontal resolution of MC-KPP is the same as the MetUM where it is coupled. The

148 vertical resolution of MC-KPP is very high at the surface (1.2m) and near the surface

149 (2 m over the first 41.5 m), since the MC-KPP columns with 100 levels over a depth of

150 1000 m are defined using a stretch function. MC-KPP simulates only vertical mixing

151 and does not include ocean dynamics, so the corrections for temperature and salinity

152 based on the seasonally-varying 3-dimension temperature and salinity flux are

153 prescribed to represent the mean ocean advection and account for biases in atmospheric

154 surface heat and fresh water fluxes. The atmospheric and oceanic components are

155 coupled every three hours. The air–sea coupling is limited by the maximum extent of a

156 seasonally varying sea ice climatology (Hirons et al. 2015). These models are

157 computationally cheaper than models with a fully interactive ocean. More important,

158 they have a smaller bias in simulated sea surface temperature (Hirons et al., 2015, Dong

159 et al. 2017; Luo et al. 2018) in comparison with fully coupled models (e.g., Wang et al.

160 2014) whilst also retaining intra-seasonal variability and coupling between the

161 atmosphere and the ocean.

162 **2.2 Experiments**

163   The experiments performed in this study are summarized in Table 1. A 12-year

164 relaxation experiment (R0) for both MetUM-GOML1 and MetUM-GOML2 models

165 was firstly performed in which the MC-KPP profiles of temperature and salinity were

166 relaxed to a present day (PD, 1994-2011) ocean temperature and salinity climatology

167 derived from the Met Office ocean analysis (Smith and Murphy 2007). The relaxation

168 experiment used PD anthropogenic greenhouse gas (GHG) and anthropogenic aerosol

169 (AA) forcings (Lamarque et al. 2010; 2011). The daily mean seasonal cycle of ocean

170 temperature and salinity corrections from the coupled relaxation experiment are then

171 imposed in free-running coupled experiments. Three other time-sliced experiments

172 using both models are performed by using different forcings, i.e. C-EP experiment

173 forced by the early period (EP, 1964–1981) mean GHG concentrations and AA

174 emissions, C-PD experiment forced by the PD (1994–2011) mean GHG concentrations

175 and AA emissions, C-FP experiment forced by future period (FP, 2045-2055) mean

176 GHG concentrations and AA emissions under the scenario of representative

177 concentration pathway (RCP) 4.5. The single RCP4.5 scenario is   chosen for

178   projection because the radiative forcings in the four scenarios of RCP2.6, RCP4.5,

179   RCP6.0, and RCP8.5 do not differ significantly in the FP of the mid—21st century

180   (Moss et al., 2010). Relative to PD means, FP mean GHG concentrations increase (CO_2

181   by 30%, CH_4 by 4.5%, and N_2O by 10.4%) and the emission of sulfur dioxide, which

182   is one of the most important aerosol species, decreases over the Europe (by 74%), the

183   East Asia (by 79%), and the North America (by 81%) but increases over Indian sub-

184   continent (Fig. 1). All experiments are run for 50 years and use the climatological PD

185   sea ice extent from the Met Office Hadley Center Sea Ice and Sea Surface Temperature

186   data set (HadISST; Rayner et al. 2003). The last 45 years of each experiment are used

187   for analysis.

188   **3. Model simulated extended summer seasonal mean surface air temperatures**

189   **and HWs**

190   **3.1 Model performance in simulating early period surface air temperatures**

191   The climatological means of daily maximum temperature (Tmax) and daily

192   minimum temperature (Tmin) in the C-EP experiments of MetUM-GOML1 and

193   MetUM-GOML2 for the extended summer are compared with the observed ones during

194   EP (Fig. 2). The observational data used is the homogenized datasets of daily Tmax and

195   Tmin series at 753 stations in China (Li et al. 2016). The observed Tmax pattern shows

196   more or less uniform distributions over southeastern China with value higher than 28 °C

197   and apparent meridional gradient over northeastern China. Over western China, a low

198   value centre locates over the Tibetan Plateau and a high value centre is over

199   northwestern China with temperature above 28 °C (Fig. 2a). The observed

200   climatological Tmin exhibits great meridional gradient over eastern China with the

201   maximum higher than 22 °C in the southeast coast of China and minimum of 4-7 °C

202   over northeastern China. The spatial distribution of Tmin over western China shows a

203   minimum (less than 1 °C) over the Tibetan Plateau and a high value (more than 16 °C)

204   over northwestern China, being similar to the spatial pattern in Tmax (Fig. 2b). The

205   spatial patterns of climatological extended summer means of Tmax and Tmin and

206   regional magnitudes in the C-EP experiments of MetUM-GOML1 and MetUM-

207   GOML2 agree well with the observed ones with pattern correlation coefficients of 0.85

208   and 0.86 for Tmax and 0.90 and 0.91 for Tmin (Fig. 2c-f). The two models reproduce

209   the observed Tmax distributions over the southeastern and northwestern part of China

210   with value above 28 °C, but slightly underestimate Tmax over the Tibetan Plateau and

211   northeastern China (Fig. 2c and e). The observed Tmin distributions are also well

212   simulated by the model, with some underestimation over the Tibetan Plateau (Fig. 2d).

213   **3.2 HWs definition**

214   Three types of HWs, namely compound, daytime, and nighttime HWs, are defined

215   in this study in the same way as the former study on decadal changes across the mid-

216   1990s over China (Su and Dong 2019). Considering the various climate types in China,

217   the relative threshold, which is determined by local climate and varies at different places

218   on different dates (Stefanon et al. 2012), is employed to define the heat waves over

219   China in this study, as was used in some previous studies (e.g., Li et al. 2017; Chen and

220 Li 2017; Wang et al. 2017). The relative threshold on each model calendar day is

221 calculated as the daily 90th percentile of daily Tmax or Tmin based on 15-day samples

222 centered on that day during the last 45 years of C-EP experiment (i.e. total samples

223 15*45 = 675 days, Della-Marta et al. 2007). A compound HW, continuous hot weather

224 in day and night, is defined when both Tmax and Tmin are higher than the thresholds

225 for at least three days. A daytime (nighttime) HW, continuous hot weather only in the

226 day (at night), is defined when only Tmax (Tmin) exceeds the thresholds for at least

227 three days. All these three types of HWs are independent of each other.

228 Three indicators, i.e. frequency, intensity, and duration, are used to measure the

229 HWs in a year. The frequency is represented by the accumulated occurrence of events

230 within a year. The intensity of each event is calculated by averaging the everyday

231 temperature exceedance above the threshold within an event. Particularly, the intensity

232 of compound HWs is the sum of the averaged Tmax and Tmin exceedances. The

233 duration of each event is the number of days when an event endures. The intensity and

234 duration for a year is computed by averaging the intensity and duration of events

235 occurring in that year.

236 **3.3 Model performance in simulating early period HWs**

237 The frequency, intensity, and duration of compound, daytime, and nighttime HWs

238 in the C-EP experiment of MetUM-GOML1 and MetUM-GOML2 during the extended

239 summer are compared with those in observations in the EP (Fig. S1-3). In observations,

240 the frequency, intensity, and duration of compound HWs share similar spatial patterns,

241   with relatively large values over the southeastern China and the northern margin of

242   mainland China (Fig. S1a-c). The daytime HWs in the EP are of the largest frequency

243   and duration over the western China and of the greatest intensity over the northern

244   margin of mainland China (Fig. S2a-c). The frequency and duration of nighttime HWs

245   are relatively high over the central China and the intensity of nighttime HWs are the

246   greatest over the northern margin of mainland China (Fig. S3a-c). The spatial patterns

247   of the frequency, intensity, and duration of all three types of HWs in observations are

248   well reproduced by these two models, despite the underestimation of the frequency and

249   duration of daytime HWs over the western China. The biases of the area averaged

250   indices are examined by using the relative bias, which is defined as the absolute bias

251   (model simulated index minus observational one) divided by observational index. The

252   relative biases for various regions range from -12% to -43% in MetUM-GOML1 and -

253   2% to -55% in MetUM-GOML2. According to Guo et al. (2017), which used 12 CMIP5

254   models to project the previously-defined HWs, the absolute value of the smallest

255   relative bias of the previously-defined HWs in all 12 CMIP5 models is 36.66%.

256   Comparing to their smallest relative bias, the smallest relative bias in MetUM-GOML1

257   and MetUM-GOML2 is much smaller, indicating a better ability of MetUM-GOML1

258   and MetUM-GOML2 in simulating the observed HWs. All the results above indicate

259   these two models' capability of capturing the characteristics of the HWs in observations

260   over China.

261   The good agreements in extended summer seasonal mean surface Tmax and Tmin

262   between model simulations and observations in many aspects and the models' ability

263 of capturing the characteristics of the HWs over China suggest a fidelity of using these

264 models for projecting their future changes. In addition, C-EP and C-PD experiments

265 were used to investigate the decadal changes in the East Asian summer monsoon,

266 temperature extremes over China, and HWs over China across the mid-1990s (Chen

267 and Dong 2018; Su and Dong 2019; Tian et al. 2018). It is indicated by the previous

268 studies that the circulation and precipitation over East Asia in present day and their

269 decadal changes across the mid-1990s simulated by these two models are consistent

270 with those in observations.

271 Previous studies on the HWs over China demonstrated significant observed

272 decadal changes in frequency, intensity, and spatial pattern of the compound, daytime,

273 and nighttime HWs over China across the mid-1990s (Chen and Li 2017; Chen and

274 Zhai 2017; Su and Dong 2019). Su and Dong (2019) quantified that the frequency of

275 compound HWs averaged over China in the PD almost triples that in the EP while both

276 intensity and spatial extent are nearly doubled. In addition, their analyses also indicated

277 that the changes of daytime and nighttime HWs are also significant in all three aspects,

278 though not as dramatical as changes of the compound HWs. They further attributed the

279 observed decadal changes to the changes in anthropogenic forcings. In order to compare

280 the projected future changes in context of model simulated past decadal-multidecadal

281 changes, the relative thresholds for three types of HWs in this study are based on early

282 period C-EP simulations as described in above and used in Su and Dong (2019). The

283 future changes of the HWs over China are indicated by the differences between C-FP

284 and C-PD experiments. Statistical significance of the mean changes is assessed using a

285   two tailed Student's t-test.

4. Future changes of HWs over China

4.1 Spatial patterns of future changes

288   Fig. 3 shows the projected future changes of compound HWs over China. The

289   frequency, intensity and duration of compound HWs significantly increase all over

290   China, but with different spatial patterns. The increase in frequency of compound HWs

291   over the southern part of China is greater than that over the northern part, particularly

292   with greatest increase on the southwest fringe of mainland China, showing maximum

293   changes of more than 5.0 events per year (Fig. 3a and b). The intensity changes of

294   compound HWs show much larger enhancement over the northern part of China than

295   southern part (Fig. 3c and d). The duration of compound HWs over China extends

296   longer with the largest change (more than 3.0 days) over the southeastern China, the

297   western China, and the southern part of northeastern China (Fig. 3e and f). Interestingly,

298   the compound HWs over the northern China and the Tibetan Plateau show the greatest

299   relative changes in all frequency, intensity, and duration with the largest ratios of these

300   three features in the FP to the PD (Fig. S4), but the frequency and duration of compound

301   HWs over the southern China are of much smaller relative changes though of the largest

302   absolute changes (Fig. 3). The future changes of compound HWs in MetUM-GOML1

303   and MetUM-GOML2 are consistent with each other. However, there are some slight

304   differences between them. For instance, the increase in frequency over the northwestern

305   China and the enhancement of intensity over northern China in MetUM-GOML2 (Fig.

14

306 3b, d) are a little bit stronger than those in MetUM-GOML1 (Fig. 3a, c).The high value

307 centre of increase in duration over the southern part of China is located in the

308 southeastern part of China in MetUM-GOML1 (Fig. 3e) but in the central southern part

309 in MetUM-GOML2 (Fig. 3f).

310   Future changes of daytime HWs are shown in Fig. 4. All three features of daytime

311 HWs increase significantly over most part of China. The frequency of daytime HWs

312 increases the most over the northwestern part of China and uniformly over large part of

313 eastern China with value of 1.0-2.0 events per year (Fig. 4a and b). The intensity of

314 daytime HWs is enhanced more evenly than that of compound HWs with relatively

315 high value of more than 0.6 °C/day over the southern part of China (Fig. 4c and d). The

316 duration of daytime HWs are lengthened over most part of China, particularly with

317 changes of more than 2.0 days being over the northwestern part of China (Fig. 4e and

318 f). The ratios of the frequency, intensity, and duration of daytime HWs in the FP to the

319 PD (Fig. S5) share the similar spatial patterns with the absolute changes of them (Fig.

320 4). The future changes of daytime HWs are almost the same in the two models with

321 very weak differences between them.

322   Future changes of nighttime HWs are illustrated in Fig. 5. Similar with the

323 compound and daytime HWs, all three features of nighttime HWs increase significantly

324 over China. The spatial distributions of the increase in frequency and intensity of

325 nighttime HWs are more spatial-uniform comparing to those of the compound HWs.

326 The increase in frequency of nighttime HWs over most part of China is similar in

327 magnitude, except the relatively large increase over the southern margin of mainland

328 China (more than 4.0 events per year; Fig. 5a and b). The changes in intensity of

329 nighttime HWs also show a more or less uniform increase over most part of China with

330 value of 0.3-0.6 °C/day, apart from the greater enhancement of intensity over the

331 northern margin of mainland China (Fig. 5c and d). The duration of nighttime HWs

332 extends longer relatively greatly over the Tibetan Plateau and the southeast coast of

333 China with the largest changes of more than 3.0 days over the Tibetan Plateau (Fig. 5e

334 and f). The pattern of relative changes of nighttime HWs (Fig. S6) are similar with those

335 of the absolute changes (Fig. 5), except that the frequency over the northeastern China

336 and the intensity over the southern margin of mainland China show larger relative

337 changes but smaller absolute changes, comparing to other regions. The spatial patterns

338 of future changes of nighttime HWs in MetUM-GOML1 and MetUM-GOML2 are

339 quite similar, despite some differences in intensity of changes, such as larger increases

340 in frequency over the central northern China and stronger enhancement of intensity over

341 northern margin of mainland China in MetUM-GOML2 (Fig. 5b and d).

342 **4.2 Area averaged future changes**

343   Fig. 6 shows the area averaged future changes in frequency, intensity, and duration

344 of three types of HWs over whole China and ratios of these three features in the FP

345 projection to the PD in MetUM-GOML1 and MetUM-GOML2. The area averaged

346 future changes and ratios of three types of HWs over China in MetUM-GOML1 in most

347 aspects agree with those in MetUM-GOML2.

348   For compound HWs, the future changes in frequency and duration in two models

349   are similar, but the increase in intensity in MetUM-GOML1 is slightly less than that in

350   MetUM-GOML2. The area averaged future changes in frequency, intensity and

351   duration of compound HWs over the whole mainland China are 3.66 (3.38) events per

352   year, 1.45 (1.94) °C/day, and 2.53 (2.67) days in MetUM-GOML1 (MetUM-GOML2;

353   Fig. 6a, c, and e). Compared to the compound HWs in the PD, the frequency of

354   compound HWs increases remarkably in the FP, which is about 4-5 times the one in the

355   PD, and the intensity and duration in the FP more or less double the ones in the PD (Fig.

356   6b, d, and f).

357   For the daytime HWs, the changes in frequency, intensity, and duration over whole

358   China in MetUM-GOML1 are very close to those in MetUM-GOML2, with values of

359   1.38 events per year, 0.51 °C/day, and 0.61 days in MetUM-GOML1 relative to those

360   ones of 1.82 events per year, 0.61 °C/day, and 0.96 days in MetUM-GOML2 (Fig. 6a,

361   c, and e). The future changes of daytime HWs are significant but weaker than those of

362   compound HWs. The frequency of daytime HWs in the FP increases by 60%-80%

363   relative to that in the PD, and the intensity of daytime HWs increases by around 40%,

364   and the duration of daytime HWs increases by 20%-30% (Fig. 6b, d, and f).

365   For the nighttime HWs, the changes in intensity over whole China are similar in

366   two models, with value of 0.45 °C/day in MetUM-GOML1 compared to 0.58 °C/day

367   in MetUM-GOML2 (Fig. 6c), while the changes in frequency and duration over whole

368   China in MetUM-GOML1, with values of 2.50 events per year and 1.29 days, are about

369   3/4 of those in MetUM-GOML2, which are 3.19 events per year and 1.68 days (Fig. 6a

370   and e). The future changes in nighttime HWs are slightly larger than those of daytime

371   HWs, but weaker than those of compound HWs. The frequency of nighttime HWs in

372   the FP almost doubles that in the PD, and the intensity and duration of nighttime HWs

373   in the FP increase by about 50%-60% and 30%-50% respectively relative to those in

374   the PD (Fig. 6b, d, and f).

375   In order to get more clarity on what these projected future changes of three types

376   of HWs exactly mean in context of past changes, the future changes of HWs over China

377   are compared to the past decadal changes of HWs across the mid-1990s, which are

378   indicated by the differences between PD and EP in observations (Su and Dong 2019).

379   Nearly all the projected future changes of the three types of HWs are stronger than their

380   decadal changes across the mid-1990s. Specifically, the projected future changes

381   relative to PD in frequency of compound HWs and all three aspects of daytime HWs

382   are 2-4 times the decadal changes across the mid-1990s in observations. The future

383   increase in duration of compound HWs and frequency and duration of nighttime HWs

384   are 20%-80% stronger than their decadal counterparts. These results suggest people

385   will encounter much fiercer changes of HWs over China in the near future than they

386   have experienced across the mid-1990s.

387   Summarizing the results above, all the compound, daytime, and nighttime HWs

388   over China are projected to occur more frequently with strengthened intensity and

389   elongated duration in the future. Quantitatively, the increases in all three aspects of

390   compound HWs in the FP are the most remarkable with the frequency being 4-5 times

391   that in the PD and the intensity and duration nearly doubling those in the PD. The

392   increases in all three aspects of daytime and nighttime HWs are also considerable, with

393   those of nighttime HWs larger than those of daytime HWs. The results of MetUM-

394   GOML1 and MetUM-GOML2 are similar in terms of spatial patterns and area averaged

395   quantities of the future changes in the three types of HWs over China, suggesting these

396   projected changes are robust at least for the two models used in this study.

4.3 Contributions of changes in mean state and variability to future changes of

HWs

399   Changes in HWs can arise from both a shift of the temperature distribution and

400   changes in temperature variability, such as a widening of the temperature distribution

401   (Meehl and Tebaldi, 2004; Schar et al., 2004; Lau and Nath, 2014; Schoetter et al., 2015,

402   Argueso et al. 2016; Guirguis et al., 2018). These studies suggested that both factors

403   will contribute to heat wave changes in future and indicated an important role of

404   temperature variability in shaping future HWs over North America and Europe.

405   However, the role of shift in temperature distribution and change in temperature

406   variability on future HWs changes over China have not studied. So, the respective

407   contributions of them to the future changes of HWs over China projected in the two

408   models are assessed in this subsection.

409   Fig. 7 illustrates the future changes in extended summer mean surface air

410   temperatures. Tmax increases by more than 1.5 °C over most part of China, with three

high value centres of increase over the southern, northwestern, and northeastern China (Fig. 7a and b). Tmin increases more or less uniformly over most part of China by more than 1.5°C, but with relatively large increases over the northern margin of mainland China and relatively small increases over the southern margin of mainland China (Fig. 7c and d). All these main features of changes in Tmax and Tmin are similar in both models despite some slight differences. The increase centre of Tmax over the southern China locates in the southeastern China in MetUM-GOML1 but in the central southern China in MetUM-GOML2 (Fig. 7a and b). The increase in Tmin in MetUM-GOML2 is greater than that in MetUM-GOML1 over the southern and northern margins of mainland China (Fig. 7c and d). What should be mentioned, the spatial patterns of future changes of the three types of HWs are consistent with those of surface air temperatures. For instance, the increase centres of intensity and duration of compound and daytime HWs over the southern China in the two models (Fig. 3c-f and 4c-f) corresponds well with the increase centres of Tmax (Fig. 7a and b). The large increase in the intensity of compound and nighttime HWs over the northern margins of mainland China (Fig. 3c-d and 5c-d) coheres to the great increase in Tmin over that region (Fig. 7c and d).

To obtain the mean temperature change induced and temperature variability-change induced future changes of HWs separately, the HWs in the future related to the mean temperature changes are obtained based on constructed daily surface air temperatures (Tmax and Tmin) by adding the climatological differences in extended summer mean surface air temperatures between the C-FP and C-PD experiments (Fig. 7) to daily surface air temperatures in the C-PD experiments. Then the temperature

20

433   variability-change induced future changes of HWs are obtained by subtracting the mean

434   temperature change induced future changes of HWs from the total future changes of

435   HWs, which refer to the difference between the C-FP and C-PD experiments.

436   Fig. 8 shows the total, mean temperature change induced, and temperature

437   variability-change induced future changes of three types of HWs averaged over whole

438   mainland China in MetUM-GOML1 and MetUM-GOML2. The future changes of HWs

439   predominantly result from the mean temperature change, which accounts for more than

440   79% of the total future changes. The spatial patterns of various properties in three types

441   of HWs induced by the mean temperature change and temperature variability-change

442   are also examined (not shown). The results of spatial patterns are consistent with the

443   area averaged ones. The spatial patterns of the mean temperature change induced future

444   changes of HWs are quite similar with those of the total future changes (Fig. 3-5) and

445   the temperature variability-change induced future changes of HWs are weak and only

446   significant over small sub-regions.

447   These results above indicate that the changes in mean temperature play a

448   predominant role in shaping future changes of HWs over China in MetUM-GOML1

449   and MetUM-GOML2. These are in agreement with Argueso et al. (2016) who showed

450   that seasonal mean temperature changes control future changes in heat waves in large

451   areas across the globe by using CMIP5 simulations. The subtle differences in future

452   changes of HWs in the two models also result from the slight differences in future

453   changes of mean state. The physical processes responsible for the future changes in the

454   mean surface air temperatures and subsequently the future changes of the three types

455   of HWs are discussed in next section.

5. Physical processes responsible for the simulated future changes of HWs

457   The spatial patterns of future extended-summer-mean changes of some key

458   variables in MetUM-GOML1 and MetUM-GOML2 are illustrated in Fig. 9 and 10. The

459   main features of changes of the physical variables in the two models are similar. The

460   most important features are increased surface downward longwave (LW) radiations

461   everywhere (Fig. 9a and b), partly induced by the increase in GHG concentrations via

462   the greenhouse effect and partly induced by the increase in water vapor in the

463   atmosphere (Fig. 10a and b). The relatively large increase of downward LW radiation

464   by about 7-9 W m^{-2} over the eastern part of China is consistent with large increase of

465   water vapor in the atmosphere by more than 3 kg m^{-2}, where the moisture transport from

466   ocean to land is enhanced (not shown) due to strengthened East Asian Summer

467   Monsoon (EASM) and more evaporation of the ocean under the warming climate. Both

468   the increased GHG concentrations and decreased AA emissions increase the land-sea

469   thermal contrast by warming land more than ocean and enhance the EASM (not shown).

470   This response of circulation is consistent with the previous studies (Lau and Kim 2017;

471   Lau et al. 2017). The relatively large increases in surface downward LW radiation over

472   the northern margin of China by 9-11 W m^{-2} are mainly the direct impacts of increased

473   greenhouse effect (Fig. 9a and b) since the increase in water vapor in the atmosphere

474   here is relatively small than other regions (Fig. 10a and b) and land surface and

475　atmospheric feedbacks are weak due to the very dry underlying surface (Dong et al.

476　2009).

477　　The changes of net surface shortwave (SW) radiation indicate an increase over

478　most part of China (Fig. 9c and d). This increase is contributed to by the increase of

479　surface clear SW radiation over southeastern and northeastern China (Fig. 9e and f) and

480　the positive anomalies of shortwave cloud radiative effect (SW CRE) over most part of

481　China (Fig. 9g and h). The increase of surface clear SW radiation over southeastern and

482　northeastern China is induced by the reduction of total aerosol optical depth (AOD; Fig.

483　10c and d) through aerosol-radiation interaction, which is primarily due to the decrease

484　of sulfur dioxide emissions (Fig. 1).

485　　The positive anomalies of SW CRE over most part of China (Fig. 9g and h) result

486　from both the decrease in cloud cover over most part of China (Fig. 10e and f) and the

487　change of cloud radiative property due to the reduction of aerosol emissions over

488　southeastern and northeastern China through cloud albedo effect of aerosol-cloud

489　interaction (Twomey 1977). From the perspective of change of cloud radiative property,

490　the decrease in aerosol emissions over southeastern and northeastern China leads to an

491　increase in the cloud droplet size (not shown) and a decrease in the cloud droplet

492　number concentration (not shown), resulting in the decrease in the reflectance of clouds

493　and the positive anomalies of SW CRE relative to the high aerosol emissions during

494　PD. From the perspective of decrease in cloud cover, different physical processes are

495　responsible for the decreases in cloud cover over different sub-regions. Over

496 northwestern China, the reduction of cloud cover is induced by decrease in relative

497 humidity (Fig. 10g and h), which under the global warming scenario is attributed to that

498 water vapor in the atmosphere over land is mainly controlled by transport from ocean

499 and constrained by ocean warming and increases less than saturation specific humidity

500 following the Clausius-Clapeyron relationship because stronger warming over land

501 than over ocean (e.g., Dong et al. 2009; Boé and Terray 2014). Over southeastern China,

502 the cloud cover is decreased by cloud lifetime effect of aerosol-cloud interaction

503 (Albrecht 1989). Over northeastern China, the reduction of cloud cover is caused by

504 both decrease in relative humidity and cloud lifetime effect of aerosol-cloud interaction.

505 In summary, the surface air temperature during extended summer over China in

506 the mid-21st century is raised by the increase in surface downward LW radiation related

507 to the enhanced greenhouse effect and the increased water vapor in the atmosphere over

508 China, resulting from the enhanced EASM and increased evaporation from ocean, and

509 by the increase in surface SW radiation related to the decreased cloud cover over most

510 part of China and the decreased AOD southeastern and northeastern China. These

511 physical processes responsible for the future increases in surface air temperature over

512 China are almost the same in MetUM-GOML1 and MetGOML2. As a result, all three

513 aspects of compound, daytime, and nighttime HWs over China would increase in the

514 future.

515 The slight differences in the changes of seasonal mean surface air temperature

516 between MetUM-GOML1 and MetUM-GOML2 are induced by the differences in the

517 increase in surface SW radiation and the increase in surface downward LW radiation,

518 which eventually lead to the subtle differences in the future changes of three types of

519 HWs. The surface SW radiation increases more over the southeastern China in MetUM-

520 GOML1 but over the central southern part of China in MetUM-GOML2 (Fig. 9b and

521 c), leading to different locations of maxmum Tmax change over that region (Fig. 7a

522 and b). The surface downward LW radiation increases more over the northern margin

523 of mainland China and central northern China in MetUM-GOML2 than in MetUM-

524 GOML1 (Fig. 9a and b), resulting in large increase in Tmin over these regions. These

525 differences in surface SW radiation and downward LW radiation are attributed to the

526 slight differences in the atmospheric circulations between the two models, since the

527 atmospheric circulations determine the aerosol distribution, water vapor transport and

528 large-scale precipitation, which have direct or indirect effects on the energy budgets.

529 **6. Conclusions**

530 The future changes in the compound, daytime, and nighttime HWs over China

531 during extended summer (May–September) in the mid-21st century (FP, 2045-2055)

532 under RCP4.5 scenario relative to present day (PD, 1994-2011) are investigated in the

533 aspects of frequency, intensity, and duration in this study. The numerical experiments

534 performed by two coupled models, comprising the atmospheric components of two

535 state-of-the-art climate models coupled to a multi-level mixed-layer ocean model and

536 having much smaller sea surface temperature biases than fully coupled general

537 circulation models, are used to evaluate the future changes in the HWs and to reveal the

538 physical processes associated with these changes. The principal results are concluded

539 below.

540   The three types of HWs over China are projected to be of more frequent

541 occurrence with strengthened intensity and elongated duration under the scenario of

542 increased GHG concentrations and decreased aerosol emissions over Eurasian

543 continent. The change in compound HWs will be the most dramatic in all three aspects,

544 with the frequency in the FP being 4-5 times that in the PD, and the intensity and

545 duration nearly doubling those in the PD. The changes of daytime and nighttime HWs

546 are also remarkable, with the increase of nighttime HWs being larger than those of

547 daytime HWs. The projected future changes of HWs over China are predominantly

548 determined by the changes in seasonal mean surface air temperatures (Tmax and Tmin)

549 with changes in temperature variability playing a minor role in both models.

550   The surface air temperatures are raised by increased downward LW radiation and

551 increased surface SW radiation, which therefore increases the frequency, intensity, and

552 duration of all three types of HWs over China. The increase in surface downward LW

553 radiation is induced by the enhanced greenhouse effect and the increased water vapor

554 in the atmosphere, resulting from the enhanced EASM and increased ocean evaporation

555 in the warming climate. The increase in surface SW radiation is contributed to, partly

556 by the decreased cloud cover due to the reduced relative humidity in a warming world

557 and partly by the decreased aerosol emissions via direct aerosol-radiation interaction

558 and indirect aerosol-cloud interaction over southeastern and northeastern China.

559   The future changes of the three types of HWs over China in MetUM-GOML1 and

560   MetUM-GOML2 are consistent in terms of spatial pattern and area averaged quantities.

561   Although slight differences exist in these future changes between two models, the

562   projected increase in frequency, intensity, and duration of the three types of HWs over

563   China under RCP4.5 scenario is robust among the two models used in this study.

564   Projected future changes of the three types of HWs in the mid-21st century relative

565   to present day are stronger than their decadal changes across the mid-90s. Specifically,

566   the projected future changes relative to PD in frequency of compound HWs and all

567   three aspects of daytime HWs are 2-4 times of the decadal changes across the mid-

568   1990s in observations. The future increase in duration of compound HWs and frequency

569   and duration of nighttime HWs are 20%-80% stronger than their decadal changes across

570   the mid-1990s. These results suggest people will encounter much fiercer changes of

571   HWs over China in the future than they have experienced across the mid-1990s and

572   China would face a challenge to take adaptation measures to cope with the projected

573   frequency increase, intensity enhancement and duration lengthening of HWs.

574   The future changes of HWs over China in the mid-21st century are projected under

575   RCP4.5 scenario in this paper. There are some other factors influencing the HWs on

576   the other timescales. For example, the variations of western North Pacific Subtropical

577   High, East Asian Jet Stream, and El Nino-Southern Oscillation have an impact on the

578   interannual variability of the HWs over China (Wang et al., 2013; Wang et al., 2016;

579   Luo and Lau, 2017; Luo and Lau, 2018). These factors should be taken into

580   consideration when forecasting the HWs on a shorter time scale.

590

Reference

Albrecht, B. A. (1989) Aerosols, cloud microphysics, and fractional cloudiness. *Science*, **245**(4923), 1227-1230, https://doi.org/10.1126/science.245.4923.1227.

Argueso, D., A. Di Luca, S. E. Perkins- Kirkpatrick and J. P. Evans (2016) Seasonal mean temperature changes control future heat waves. *Geophys. Res. Lett.*, **43**(14), 7653-7660, https://doi.org/10.1002/2016GL069408.

Arribas, A., M. Glover, A. Maidens, K. Peterson, M. Gordon, C. MacLachlan, R. Graham, D. Fereday, J. Camp and A. Scaife (2011) The GloSea4 ensemble prediction system for seasonal forecasting. *Mon. Wea. Rev.*, **139**(6), 1891-1910, https://doi.org/10.1175/2010MWR3615.1.

Black, E., M. Blackburn, G. Harrison, B. Hoskins and J. Methven (2004) Factors contributing to the summer 2003 European heatwave. *Weather*, **59**(8), 217-223, https://doi.org/doi:10.1256/wea.74.04.

Boé, J. and L. Terray (2014) Land–sea contrast, soil-atmosphere and cloud-temperature interactions: interplays and roles in future summer European climate change. *Clim. Dyn.*, **42**(3-4), 683-699, https://doi.org/10.1007/s00382-013-1868-8.

Chen, R. D. and R. Y. Lu (2014) Large-scale circulation anomalies associated with 'tropical night' weather in Beijing, China. *Int. J. Climatol.*, **34**(6), 1980-1989, https://doi.org/10.1002/joc.3815.

Chen, W. and B. Dong (2018) Anthropogenic impacts on recent decadal change in temperature extremes over China: relative roles of greenhouse gases and anthropogenic aerosols. *Clim. Dyn.*, https://doi.org/10.1007/s00382-018-4342-9.

Chen Y., W. Chen, Q. Su, F. Luo, S. Sparrow, F. Tian, B. Dong, S. F. B. Tett, F. C. Lott, and D. Wallom (2018) Anthropogenic warming has substantially increased the likelihood of July 2017-like heat waves over Central-Eastern China [in "Explaining Extremes of 2017 from a Climate Perspective"]. Acepted by *Bull. Amer. Meteor. Soc.*.

Chen, Y. and Y. Li (2017) An inter-comparison of three heat wave types in China during 1961-2010: Observed basic features and linear trends. *Sci. Rep.*, **7**, 45619, https://doi.org/10.1038/srep45619.

Chen, Y. and P. Zhai (2017) Revisiting summertime hot extremes in China during 1961- 2015: overlooked compound extremes and significant changes. *Geophys. Res. Lett.*, **44**(10), https://doi.org/10.1002/2016GL072281.

Coumou, D. and S. Rahmstorf (2012) A decade of weather extremes. *Nat. Clim. Change*, **2**(7), 491-496, https://doi.org/10.1038/nclimate1452.

Della-Marta, P. M., J. Luterbacher, H. von Weissenfluh, E. Xoplaki, M. Brunet and H. Wanner (2007) Summer heat waves over western Europe 1880–2003, their relationship to large-scale forcings and predictability. *Clim. Dyn.*, **29**(2), 251-275,

629   https://doi.org/10.1007/s00382-007-0233-1.

630   Dong, B., J. M. Gregory and R. T. Sutton (2009) Understanding land–sea warming
631   contrast in response to increasing greenhouse gases. Part I: Transient adjustment.
632   *J. Clim.*, **22**(11), 3079-3097, https://doi.org/10.1175/2009JCLI2652.1.

633   Dong, B., R. T. Sutton, L. Shaffrey and N. P. Klingaman (2017) Attribution of forced
634   decadal climate change in coupled and uncoupled ocean–atmosphere model
635   experiments. *J. Clim.*, **30**(16), 6203-6223, https://doi.org/10.1175/jcli-d-16-
636   0578.1.

637   Freychet, N., S. Tett, J. Wang and G. Hegerl (2017) Summer heat waves over Eastern
638   China: dynamical processes and trend attribution. *Environ. Res. Lett.*, **12**(2),
639   024015, https://doi.org/10.1088/1748-9326/aa5ba3.

640   Freychet, N., S. Sparrow, S. F. B. Tett, M. J. Mineter, G. C. Hegerl and D. C. H. Wallom
641   (2018) Impacts of anthropogenic forcings and El Nino on Chinese extreme
642   temperatures. *Adv. Atmos. Sci.*, **35**(8), 994-1002, https://doi.org/10.1007/s00376-
643   018-7258-8.

644   Gershunov, A., D. R. Cayan and S. F. Iacobellis (2009) The great 2006 heat wave over
645   California and Nevada: signal of an increasing trend. *J. Clim.*, **22**(23), 6181-6203,
646   https://doi.org/10.1175/2009JCLI2465.1.

647   Guirguis, K., A. Gershunov, D. R. Cayan and D. W. Pierce (2018) Heat wave
648   probability in the changing climate of the Southwest US. *Clim. Dyn.*, **50**(9-10),
649   3853-3864, https://doi.org/10.1007/s00382-017-3850-3.

650   Gosling, S. N., J. A. Lowe, G. R. McGregor, M. Pelling and B. D. Malamud (2009)
651   Associations between elevated atmospheric temperature and human mortality: a
652   critical review of the literature. *Climatic Change*, **92**(3-4), 299-341,
653   https://doi.org/10.1007/s10584-008-9441-x.

654   Guo, X., J. Huang, Y. Luo, Z. Zhao and Y. Xu (2017) Projection of heat waves over
655   China for eight different global warming targets using 12 CMIP5 models. *Theor.*
656   *Appl. Climatol.*, **128**(3-4), 507-522, https://doi.org/10.1007/s00704-015-1718-1.

657   Hatfield, J. L. and J. H. Prueger (2015) Temperature extremes: Effect on plant growth
658   and development. *Weather and Climate Extremes*, **10**, 4-10,
659   https://doi.org/10.1016/j.wace.2015.08.001.

660   Hirons, L., N. Klingaman and S. Woolnough (2015) MetUM-GOML: a near-globally
661   coupled atmosphere–ocean-mixed-layer model. *Geosci. Model Dev.*, **8**, 363-379,
662   https://doi.org/10.5194/gmd-8-363-2015.

663   Jones, C., et al (2011) The HadGEM2-ES implementation of CMIP5 centennial
664   simulations. *Geosci. Model Dev.*, **4**(3), 543–570, https://doi.org/10.5194/gmd-4-
665   543-2011.

666   Karl, T. R. and R. W. Knight (1997) The 1995 Chicago heat wave: How likely is a

667 recurrence? *Bull. Amer. Meteor. Soc.*, **78**(6), 1107-1120,
668 https://doi.org/10.1175/1520-0477(1997)078<1107:tchwhl>2.0.co;2.

669 Lamarque, J.-F., G. P. Kyle, M. Meinshausen, K. Riahi, S. J. Smith, D. P. van Vuuren,
670 A. J. Conley and F. Vitt (2011) Global and regional evolution of short-lived
671 radiatively-active gases and aerosols in the Representative Concentration
672 Pathways. *Climatic Change*, **109**, 191, https://doi.org/10.1007/s10584-011-0155-
673 0.

674 Lamarque, J.-F., T. C. Bond, V. Eyring, C. Granier, A. Heil, Z. Klimont, D. Lee, C.
675 Liousse, A. Mieville and B. Owen (2010) Historical (1850–2000) gridded
676 anthropogenic and biomass burning emissions of reactive gases and aerosols:
677 methodology and application. *Atmos. Chem. Phys.*, **10**(15), 7017-7039,
678 https://doi.org/10.5194/acp-10-7017-2010.

679 Lau, N.-C., and M. J. Nath (2014) Model simulation and projection of European heat
680 waves in present-day and future climates, *J. Clim.*, **27**(10), 3713–3730,
681 https://doi.org/10.1175/jcli-d-13-00284.1.

682 Lau, W. K. M., K. M. Kim and L. R. Leung (2017) Changing circulation structure and
683 precipitation characteristics in Asian monsoon regions: greenhouse warming vs.
684 aerosol effects. *Geosci. Lett.*, **4**(1), 28, https://doi.org/10.1186/s40562-017-0094-
685 3.

686 Lau, W. K. M. and K. M. Kim (2017) Competing influences of greenhouse warming
687 and aerosols on Asian summer monsoon circulation and rainfall. *Asia-Pac. J. Atmo.
688 Sci.,* **53**(2), 181-194, https://doi.org/10.1007/s13143-017-0033-4.

689 Lesk, C., P. Rowhani and N. Ramankutty (2016) Influence of extreme weather disasters
690 on global crop production. *Nature*, **529**(7584), 84,
691 https://doi.org/10.1038/nature16467.

692 Li, Y., Y. Ding and W. Li (2017) Observed trends in various aspects of compound heat
693 waves across China from 1961 to 2015. *J. Meteor. Res.*, **31**(3), 455-467,
694 https://doi.org/10.1007/s13351-017-6150-2.

695 Li, Z., L. J. Cao, Y. N. Zhu and Z. W. Yan (2016) Comparison of two homogenized
696 datasets of daily maximum/mean/minimum temperature in China during 1960-
697 2013. *J. Meteor. Res.*, **30**(1), 53-66, https://doi.org/10.1007/s13351-016-5054-x.

698 Luo, F., B. Dong, F. Tian and S. Li (2018). Anthropogenically forced decadal change
699 of South Asian summer monsoon across the mid-1990s. Submitted to *J. Geophys.
700 Res. Atmos.*.

701 Luo, M. and N.-C. Lau (2017) Heat waves in southern China: Synoptic behavior, long-
702 term change, and urbanization effects. *J. Clim.*, **30**(2), 703-720,
703 https://doi.org/10.1175/jcli-d-16-0269.1.

704 Luo, M. and N.-C. Lau (2018) Synoptic characteristics, atmospheric controls, and long-
705 term changes of heat waves over the Indochina Peninsula. *Clim. Dyn.*, **51**(7-8),

2707-2723, https://doi.org/10.1007/s00382-017-4038-6.

Ma, S. M., T. J. Zhou, D. A. Stone, O. Angelil and H. Shiogama (2017) Attribution of the July-August 2013 heat event in Central and Eastern China to anthropogenic greenhouse gas emissions. *Environ. Res. Lett.*, **12**(5), https://doi.org/10.1088/1748-9326/aa69d2.

Meehl, G. A. and C. Tebaldi (2004) More intense, more frequent, and longer lasting heat waves in the 21st Century. *Science*, **305**(5686), 994-997, https://doi.org/10.1126/science.1098704.

Moss, R. H., J. A. Edmonds, K. A. Hibbard, M. R. Manning, S. K. Rose, D. P. Vuuren, Van, T. R. Carter, E. Seita, K. Mikiko and K. Tom (2010) The next generation of scenarios for climate change research and assessment. *Nature*, **463**(7282), 747-756, https://doi.org/10.1038/nature08823.

Perkins, S. E. (2015) A review on the scientific understanding of heatwaves—Their measurement, driving mechanisms, and changes at the global scale. *Atmos. Res.*, **164–165**, 242-267, https://doi.org/10.1016/j.atmosres.2015.05.014.

Perkins, S. E. and L. V. Alexander (2013) On the measurement of heat waves. *J. Clim.*, **26**(13), 4500-4517, https://doi.org/10.1175/jcli-d-12-00383.1.

Rayner NA, Parker DE, Horton EB, Folland CK, Alexander LV, Rowell DP, Kent EC, Kaplan A (2003) Global analyses of SST, sea ice and night marine air temperature since the late nineteenth century. J Geophys Res 108. doi:10.1029/2002JD002670

Robine, J.-M., S. L. K. Cheung, S. Le Roy, H. Van Oyen, C. Griffiths, J.-P. Michel and F. R. Herrmann (2008) Death toll exceeded 70,000 in Europe during the summer of 2003. *C. R. Biol.*, **331**(2), 171-178, https://doi.org/10.1016/j.crvi.2007.12.001.

Seneviratne, S. I., M. G. Donat, B. Mueller and L. V. Alexander (2014) No pause in the increase of hot temperature extremes. *Nat. Clim. Change*, **4**(3), 161, https://doi.org/10.1038/nclimate2145.

Schär, C., P. L. Vidale, D. Lüthi, C. Frei, C. Häberli, M. A. Liniger, and C. Appenzeller (2004), The role of increasing temperature variability in European summer heatwaves, *Nature*, *427*(6972), 332–336, https://doi.org/10.1038/nature02300.

Schoetter, R., J. Cattiaux and H. Douville (2015) Changes of western European heat wave characteristics projected by the CMIP5 ensemble. *Clim. Dyn.*, **45**(5-6), 1601-1616, https://doi.org/10.1007/s00382-014-2434-8.

Smith, D. M. and J. M. Murphy (2007) An objective ocean temperature and salinity analysis using covariances from a global climate model. *J. Geophys. Res. Oceans*, **112**(C2), https://doi.org/10.1029/2005JC003172.

Sparrow, S., Q. Su, F. X. Tian, S. H. Li, Y. Chen, W. Chen, F. F. Luo, N. Freychet, F. C. Lott, B. W. Dong, S. F. B. Tett and D. Wallom (2018) Attributing human influence on the July 2017 Chinese heatwave: the influence of sea-surface temperatures.

Environ. Res. Lett., **13**(11), https://doi.org/10.1088/1748-9326/ade356.

Stefanon, M., D. A. Fabio and D. Philippe (2012) Heatwave classification over Europe and the Mediterranean region. *Environ. Res. Lett.*, **7**(1), 014023, https://doi.org/10.1088/1748-9326/7/1/014023.

Su, Q. and B. Dong (2019) Recent decadal changes in heat waves over China: drivers and mechanisms. Submitted to *J. Clim.*.

Sun, Y., L. Song, H. Yin, B. Zhou, T. Hu, X. Zhang and P. Stott (2016) Human influence on the 2015 extreme high temperature events in Western China [in "Explaining Extremes of 2015 from a Climate Perspective"]. *Bull. Amer. Meteor. Soc.*, **97**(12), S102-S106, https://doi.org/10.1175/bams-d-16-0158.1.

Sun, Y., X. B. Zhang, F. W. Zwiers, L. C. Song, H. Wan, T. Hu, H. Yin and G. Y. Ren (2014) Rapid increase in the risk to extreme summer heat in Eastern China. *Nat. Clim. Change*, **4**(12), 1082-1085, https://doi.org/10.1038/nclimate2410.

Tan, J., Y. Zheng, G. Song, L. S. Kalkstein, A. J. Kalkstein and X. Tang (2007) Heat wave impacts on mortality in Shanghai, 1998 and 2003. *Int. J. Biometeorol.*, **51**(3), 193-200, https://doi.org/10.1007/s00484-006-0058-3.

Tian, F., B. Dong, J. Robson and R. Sutton (2018) Forced decadal changes in the East Asian summer monsoon: the roles of greenhouse gases and anthropogenic aerosols. *Clim. Dyn.*, 1-17, https://doi.org/10.1007/s00382-018-4105-7.

Twomey, S. (1977) Influence of pollution on shortwave albedo of clouds. *J. Atmos. Sci.*, **34**(7), 1149-1152, https://doi.org/10.1175/1520-0469(1977)034<1149:tiopot>2.0.co;2.

Walters, D., M. Best, A. Bushell, D. Copsey, J. Edwards, P. Falloon, C. Harris, A. Lock, J. Manners and C. Morcrette (2011) The Met Office Unified Model global atmosphere 3.0/3.1 and JULES global land 3.0/3.1 configurations. *Geosci. Model Dev.*, **4**(4), 919, https://doi.org/10.5194/gmd-4-919-2011.

Walters, D., N. Wood, S. Vosper and S. Milton (2014) ENDGame: A new dynamical core for seamless atmospheric prediction. Met Office documentation, can be consulted at http://www.metoffice.gov.uk/media/pdf/s/h/ENDGameGOVSciv2.0.pdf.

Walters, D., M. Brooks, I. Boutle, T. Melvin, R. Stratton, S. Vosper, H. Wells, K. Williams, N. Wood and T. Allen (2017) The Met Office unified model global atmosphere 6.0/6.1 and JULES global land 6.0/6.1 configurations. *Geosci. Model Dev.*, **10**(4), 1487-1520, https://doi.org/10.5194/gmd-10-1487-2017.

Wang, C., L. Zhang, S.-K. Lee, L. Wu, and C. R. Mechoso (2014) A global perspective on CMIP5 climate model biases. *Nat. Clim. Change*, **4**, 201–205, doi:https://doi.org/10.1038/nclimate2118.

Wang, P., J. Tang, X. Sun, S. Wang, J. Wu, X. Dong and J. Fang (2017) Heatwaves in

China: definitions, leading patterns and connections to large-scale atmospheric circulation and SSTs. *J. Geophys. Res. Atmos.*, **122**(20), https://doi.org/10.1002/2017JD027180.

Wang, W., W. Zhou, X. Li, X. Wang and D. Wang (2016) Synoptic-scale characteristics and atmospheric controls of summer heat waves in China. *Clim. Dyn.*, **46**(9), 2923-2941, https://doi.org/10.1007/s00382-015-2741-8.

Wang, W., W. Zhou, X. Wang, S. K. Fong and K. C. Leong (2013) Summer high temperature extremes in Southeast China associated with the East Asian jet stream and circumglobal teleconnection. *J. Geophys. Res. Atmos.*, **118**(15), 8306-8319, https://doi.org/10.1002/jgrd.50633.

Wilbanks, T. J. and S. Fernandez (2014) Climate change and infrastructure, urban systems, and vulnerabilities: Technical report for the US department of energy in support of the national climate assessment, Island Press.

Wilcox, L. J., B. Dong, R. T. Sutton and E. J. Highwood (2015) The 2014 hot, dry summer in Northeast Asia [in "Explaining Extremes of 2014 from a Climate Perspective"]. *Bull. Amer. Meteor. Soc.*, **96**(12), S105-S110, https://doi.org/10.1175/bams-d-15-00123.1.

You, Q. L., Z. H. Jiang, L. Kong, Z. W. Wu, Y. T. Bao, S. C. Kang and N. Pepin (2017) A comparison of heat wave climatologies and trends in China based on multiple definitions. *Clim. Dyn.*, **48**(11), 3975-3989, https://doi.org/10.1007/s00382-016-3315-0.

Yu, R., P. M. Zhai and Y. Y. Lu (2018) Implications of differential effects between 1.5 and 2 degrees C global warming on temperature and precipitation extremes in China's urban agglomerations. *Int. J. Climatol.*, **38**(5), 2374-2385, https://doi.org/10.1002/joc.5340.

Zhou, B., Q. H. Wen, Y. Xu, L. Song and X. Zhang (2014a) Projected changes in temperature and precipitation extremes in China by the CMIP5 multimodel ensembles. *J. Clim.*, **27**(17), 6591-6611, https://doi.org/10.1175/jcli-d-13-00761.1.

Zhou, T. J., S. M. Ma and L. W. Zou (2014b) Understanding a hot summer in Central Eastern China: summer 2013 in context of multimodel trend analysis [in "Explaining Extremes of 2013 from a Climate Perspective"]. *Bull. Amer. Meteor. Soc.*, **95**(9), S54-S57.

815 **Table 1.** Summary of numerical experiments

Abv.	Experiment	Ocean	Radiative forcing
R0	Relaxation run	Relaxation to "present day" (PD, 1994-2011) mean 3D ocean temperature and salinity to diagnose climatological temperature and salinity tendencies	PD greenhouse gases (GHGs) over 1994~2011 and anthropogenic aerosol (AA) emissions over 1994~2010 with AA after 2006 from RCP4.5 scenario (Lamarque et al. 2010, 2011)
C-EP	Early period (EP 1964~1981)	Climatological temperature and salinity tendencies from relaxation run	EP mean GHG and EP mean AA emissions
C-PD	Present day (PD 1994~2011)		PD mean GHG and PD mean AA emissions
C-FP	future period (FP, 2045-2055)		RCP4.5 emission scenario

816
817

818

Annual sulfur dioxide (2045-2055 minus 1994-2010)
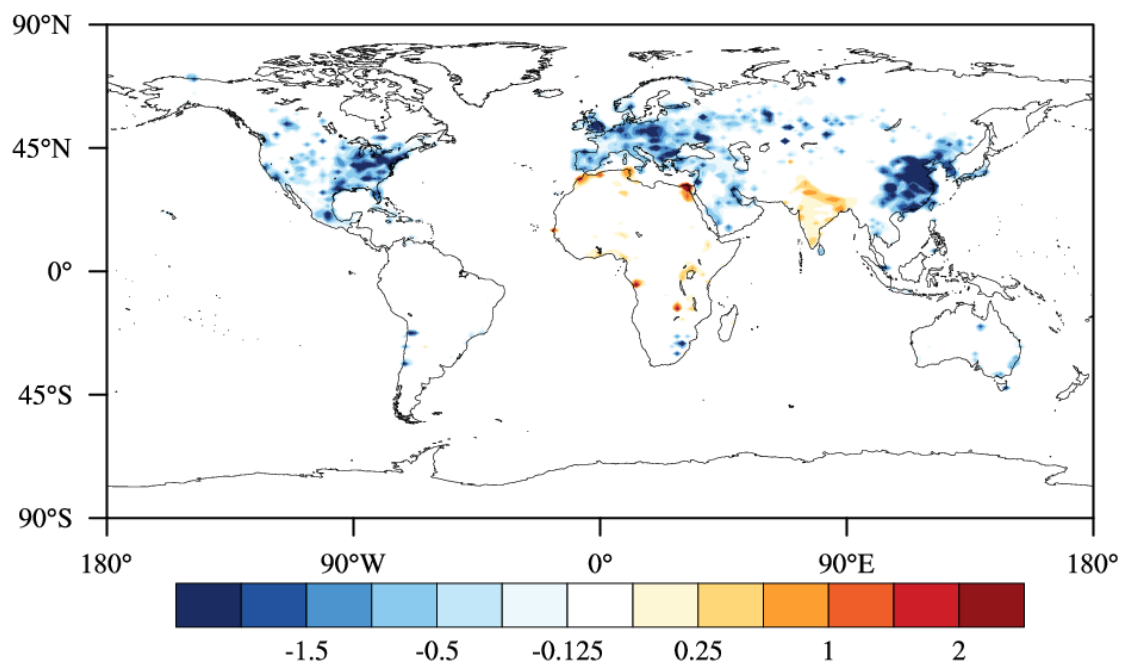
819

820 **Figure 1.** Future changes in annual mean sulfur dioxide emissions (units: g m^{-2} yr^{-1}) during the

821 mid-21st century relative to the PD of 1994-2010.

822
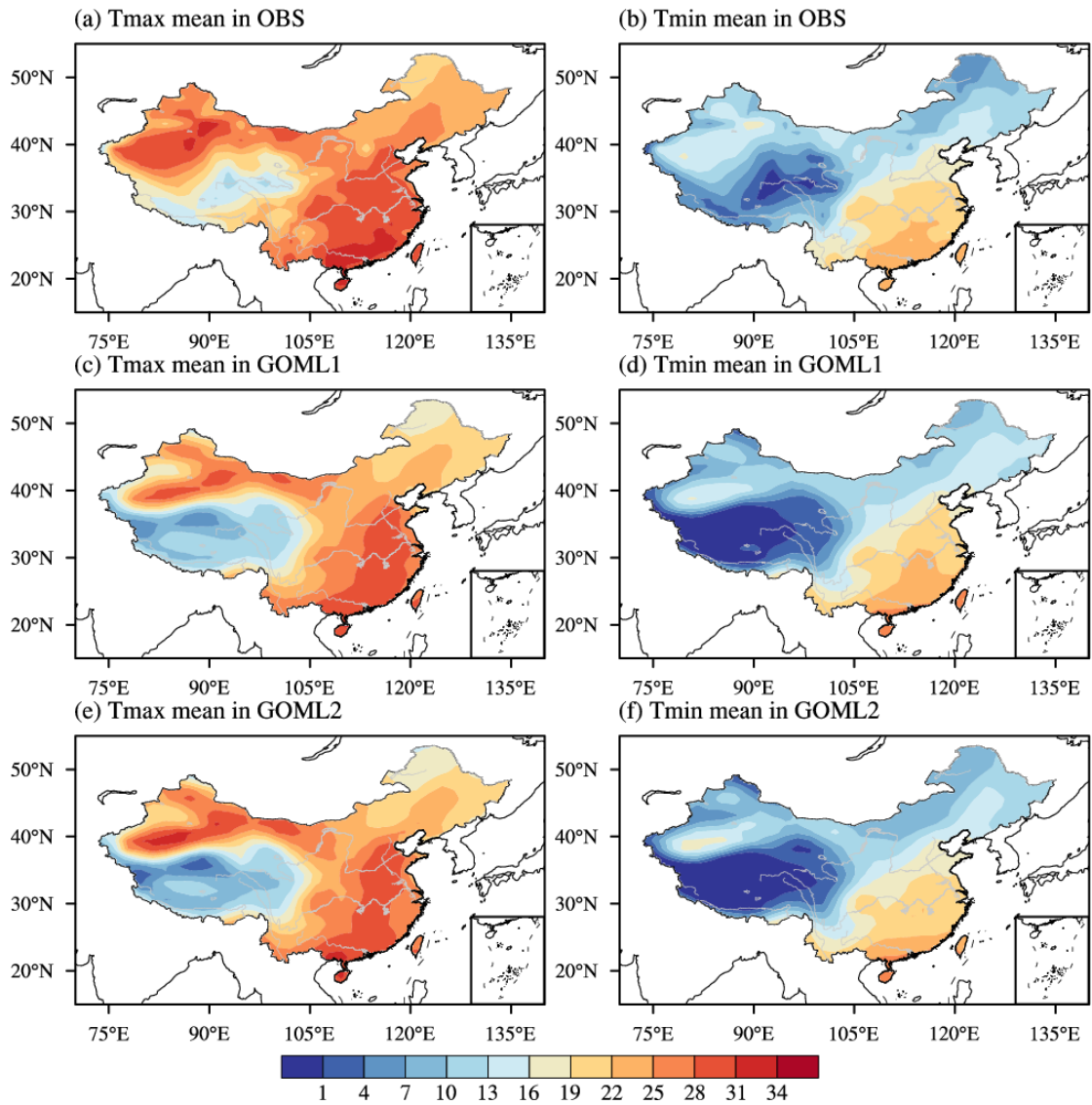
Figure 2. Climatological means of extended-summer-mean (May–September) Tmax and Tmin

during the EP (1964-1981) in observations (a and b) and in the C-EP experiment of MetUM-

GOML1 (c and d) and MetUM-GOML2 (e and f). Units are in ℃.

Compound HWs
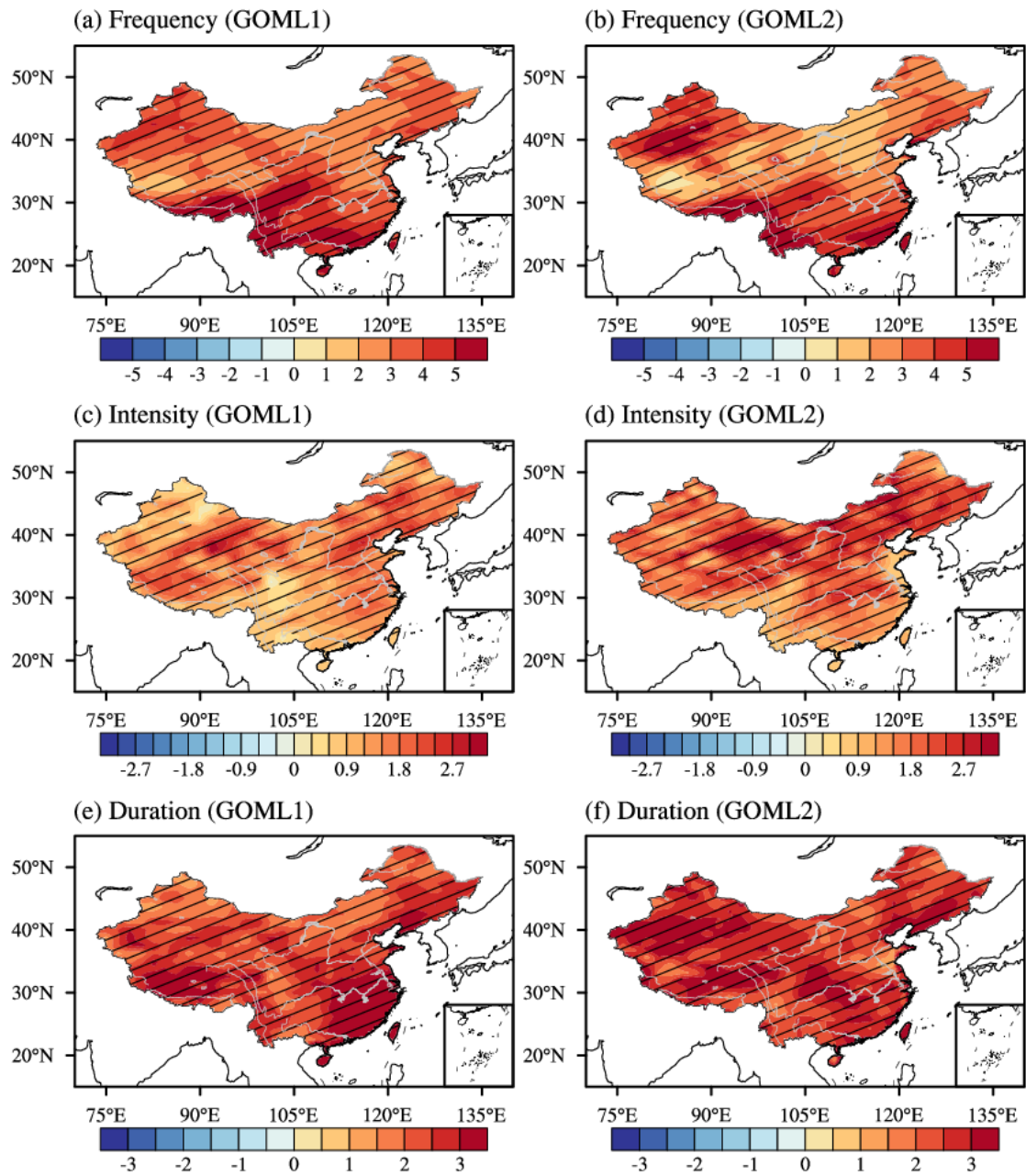
Figure 3. Spatial patterns of future changes in frequency (units: events/year; a and b), intensity

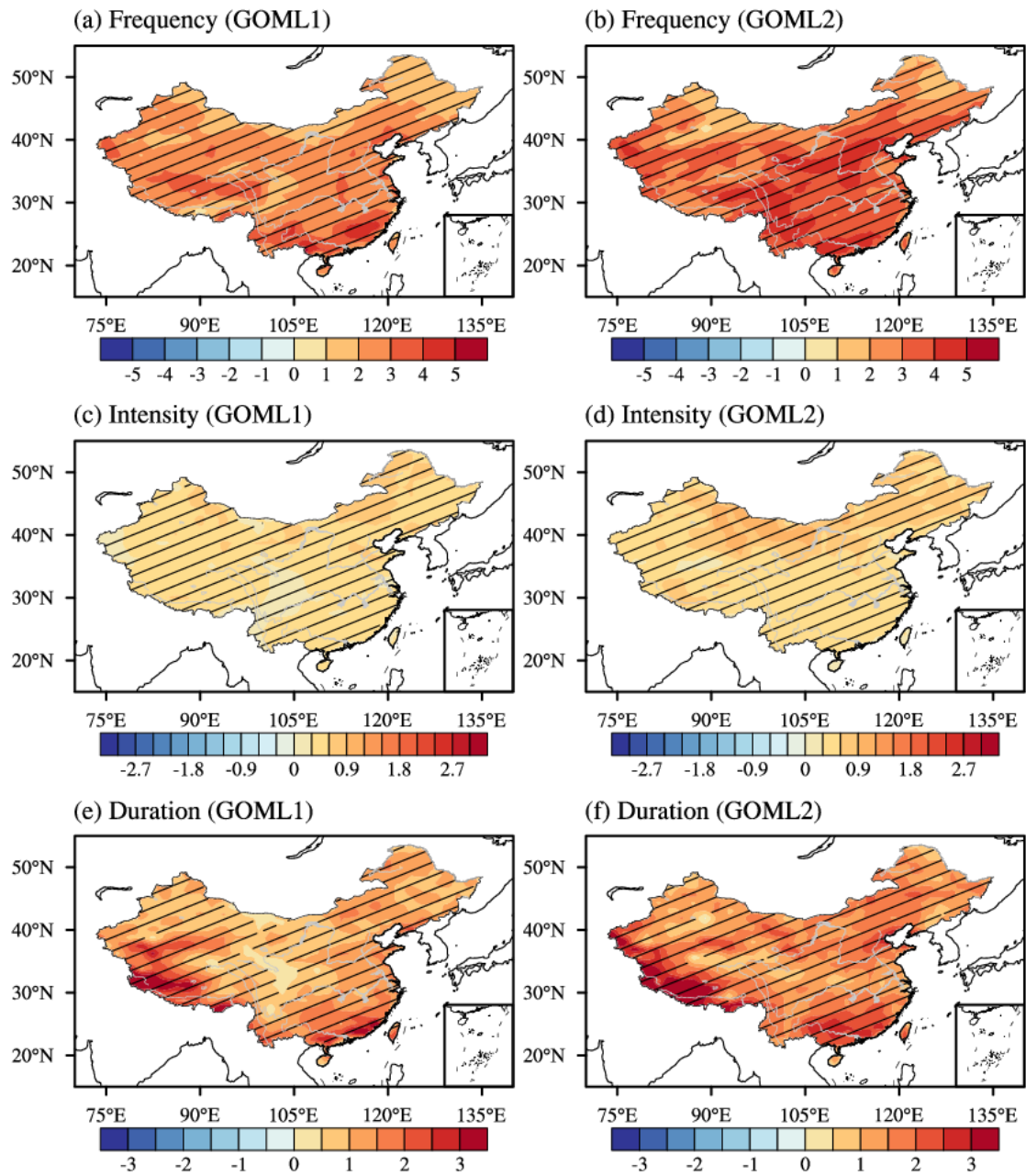(units: °C/day; c and d), and duration (units: days; e and f) of compound HWs in MetUM-GOML1

(left panels) and MetUM-GOML2 (right panels), masked by China boundary. The slashes highlight

the regions where the differences are statistically significant at the 90% confidence level based on

a two-tailed Student's *t*-test.
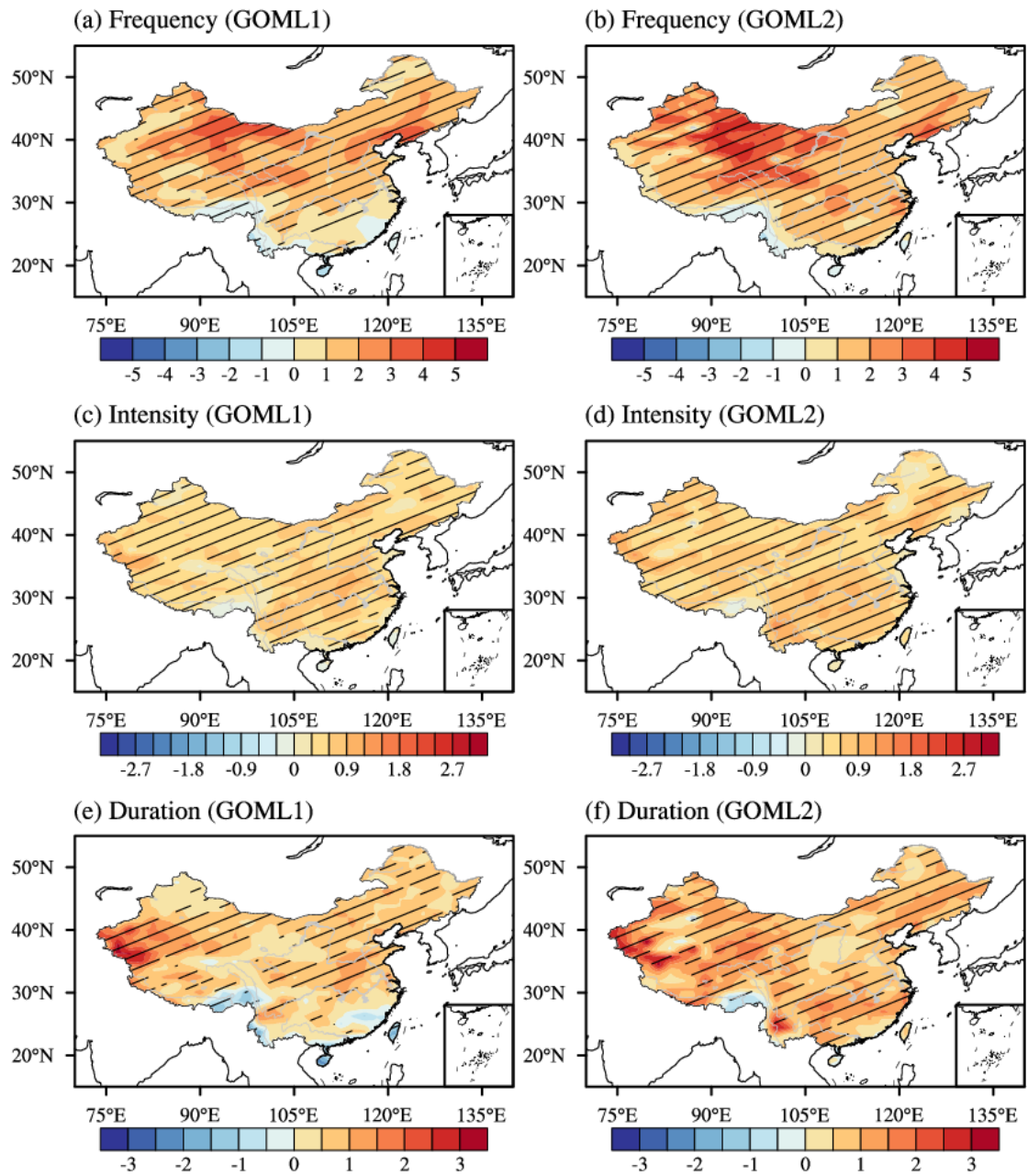
Daytime HWs

Figure 4. Spatial patterns of future changes in frequency (units: events/year; a and b), intensity

(units: °C/day; c and d), and duration (units: days; e and f) of daytime HWs in MetUM-GOML1

(left panels) and MetUM-GOML2 (right panels), masked by China boundary. The slashes highlight

the regions where the differences are statistically significant at the 90% confidence level based on
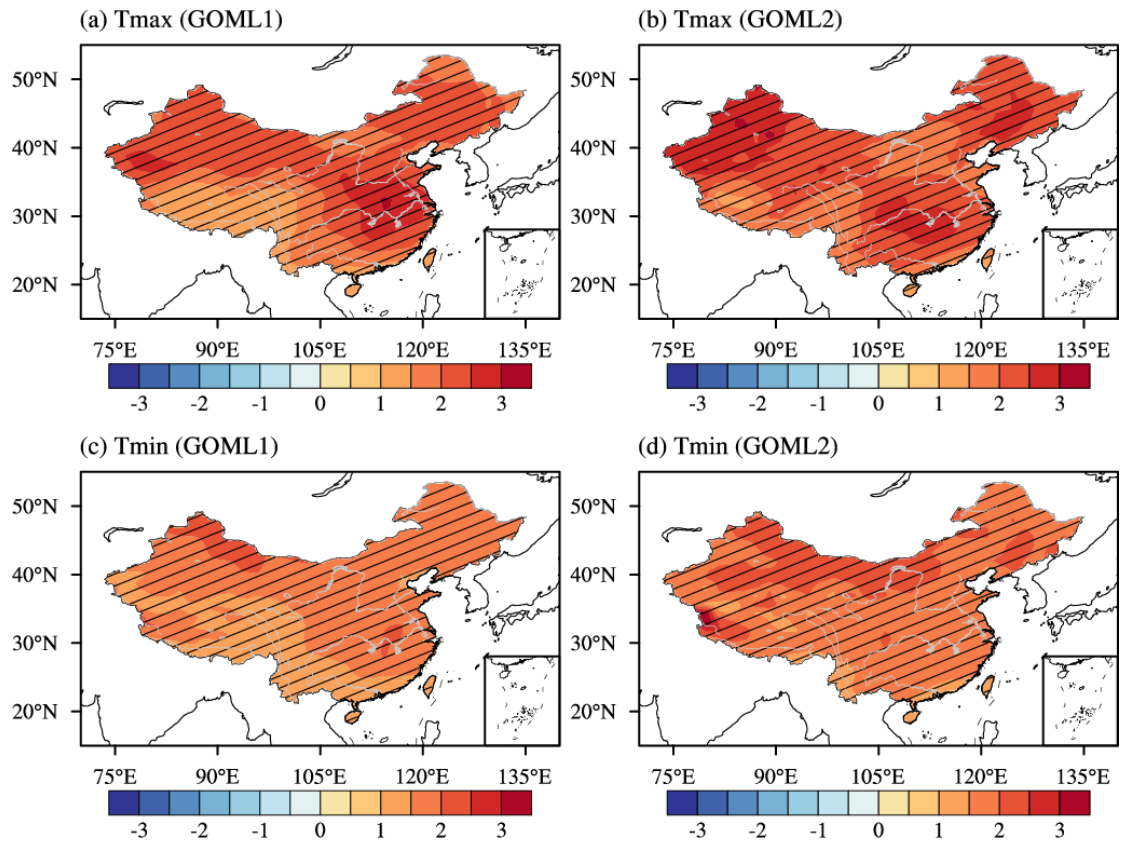
a two-tailed Student's *t*-test.

Nighttime HWs

Figure 5. Spatial patterns of future changes in frequency (units: events/year; a and b), intensity

(units: °C/day; c and d), and duration (units: days; e and f) of nighttime HWs in MetUM-GOML1

(left panels) and MetUM-GOML2 (right panels), masked by China boundary. The slashes highlight

the regions where the differences are statistically significant at the 90% confidence level based on

a two-tailed Student's *t*-test.
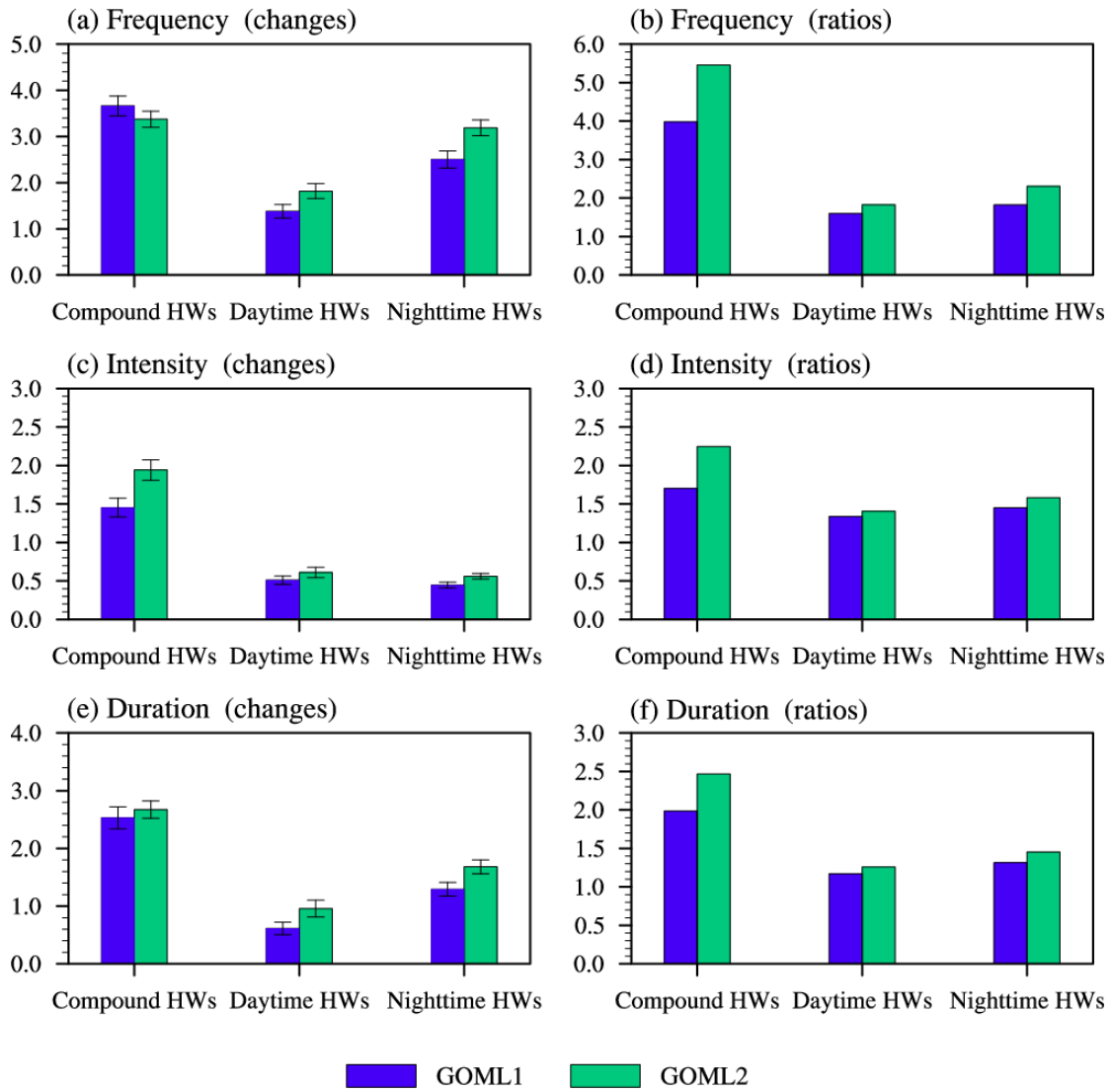
Figure 6. Area averaged future changes of frequency (a), intensity (c), and duration (e) of compound, daytime, and nighttime HWs over whole China and the ratios of these three features in the FP projection to the PD (b, d, and f) in MetUM-GOML1 and MetUM-GOML2. Units for frequency, intensity, and duration are events/year, °C/day, and days, respectively. The error bars indicate the 90% confidence intervals based on two-tailed Student's *t*-test.

856

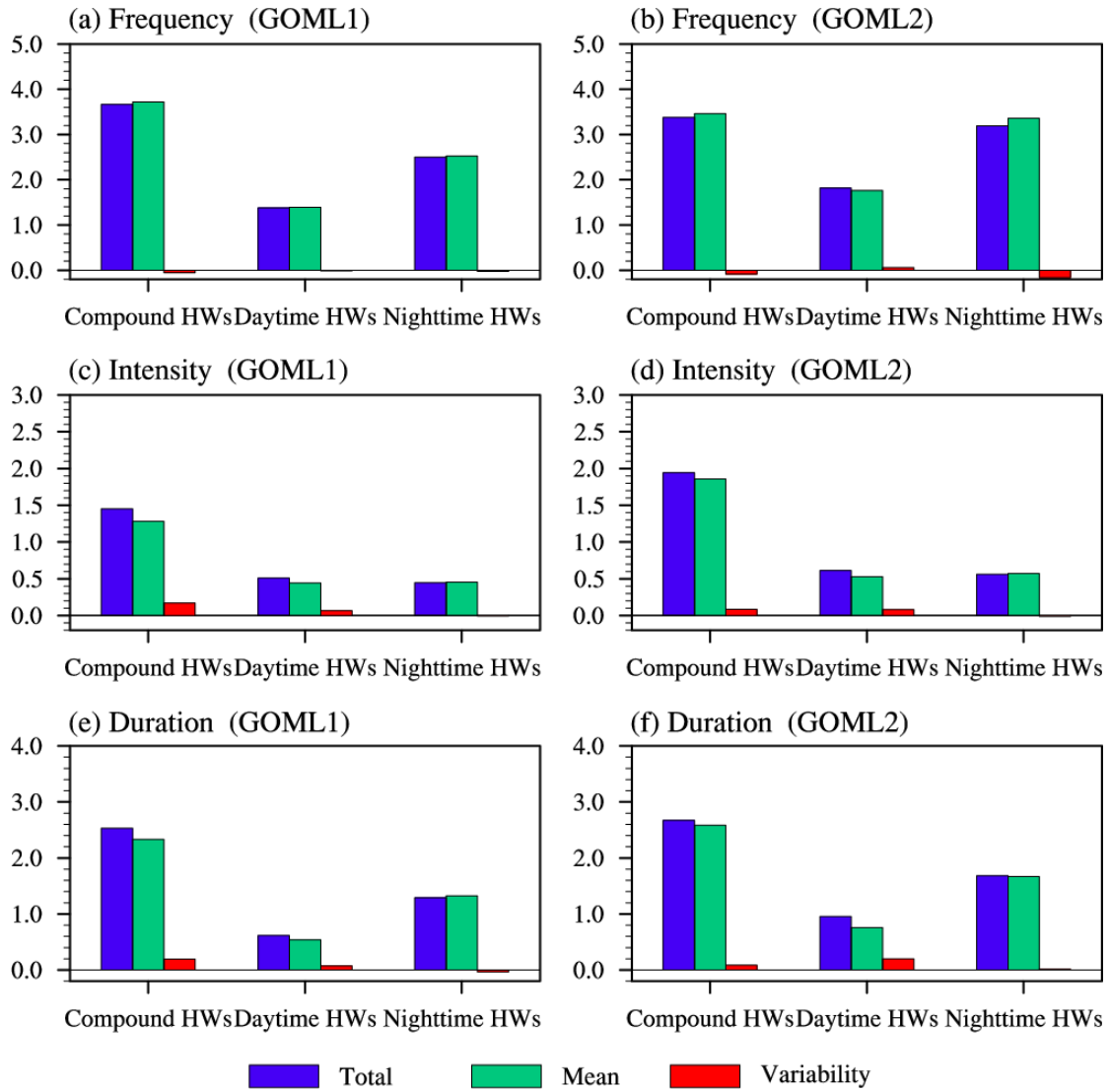857 **Figure 7.** Future changes in the extended-summer-mean (May–September) Tmax and Tmin relative

858 to PD simulations in MetUM-GOML1 (a and c) and MetUM-GOML2 (b and d). Units are in ℃.

859 The slashes highlight the regions where the differences are statistically significant at the 90%

860 confidence level based on a two-tailed Student's *t*-test.

861

862

863

Figure 8. Area averaged total, mean temperature change induced, temperature variability-change

induced future changes in frequency (units: events/year; a and b), intensity (units: °C/day; c and d),

and duration (units: days; e and f) of compound, daytime, and nighttime HWs over whole China in

MetUM-GOML1 (left panels) and MetUM-GOML2 (right panels).

868
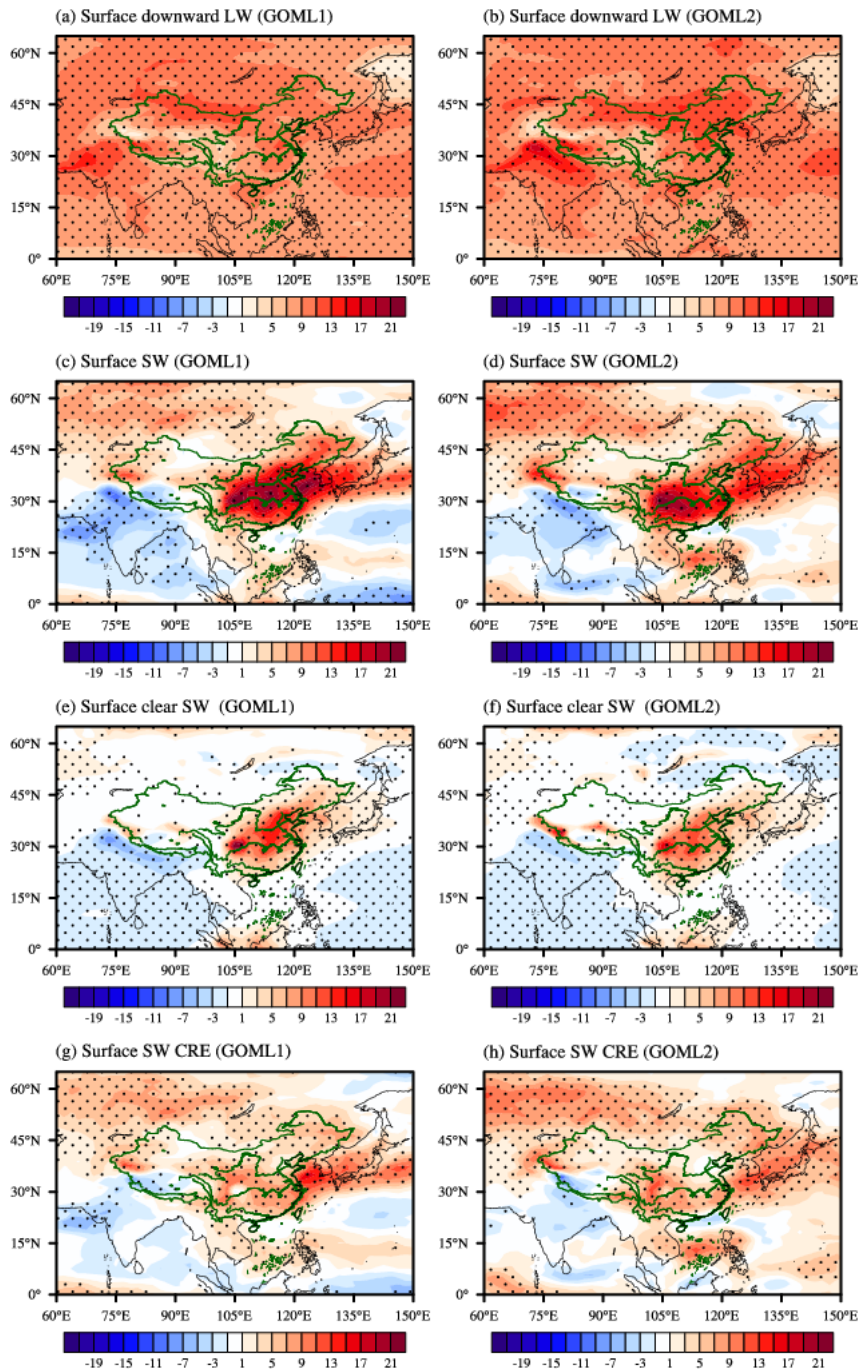
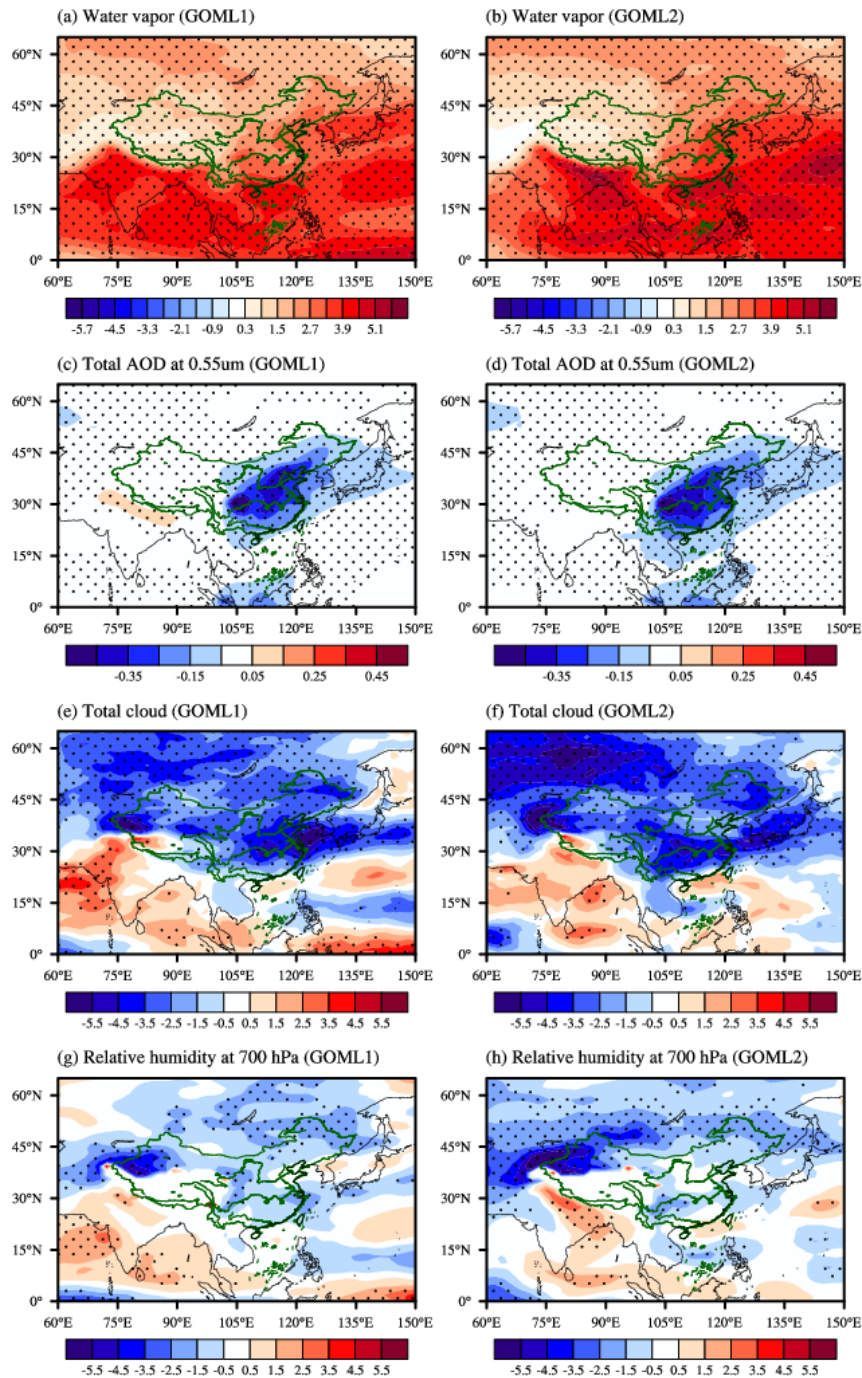**Figure 9.** Spatial patterns of future extended-summer-mean changes in surface downward LW radiation (a and b), net surface SW radiation (c and d), surface clear SW radiation (e and f), and surface SW CRE (g and h) in MetUM-GOML1 (left panels) and MetUM-GOML2 (right panels). Radiation with positive value meaning downward and in W m^{-2}. The black dots highlight regions where the changes are statistically significant at the 90% confidence level based on a two-tailed Student's *t*-test.

Figure 10. Spatial patterns of future extended-summer-mean changes in column-integrated water

vapor (a and b; units: kg m^{-2}), total AOD at 0.55 um (c and d), total cloud cover (e and f; units: %),

and relative humidity at 700 hPa (g and h; units: %) in MetUM-GOML1 (left panels) and MetUM-

GOML2 (right panels). The black dots highlight regions where the changes are statistically

significant at the 90% confidence level based on a two-tailed Student's t-test.